

# Quantum phase transitions of the diluted O(3) rotor model

Thomas Vojta

*Department of Physics, University of Missouri - Rolla, Rolla, MO 65409, USA*

Rastko Sknepnek

*Department of Physics and Astronomy, McMaster University, Hamilton ON L8S 4M1, Canada*

(Dated: May 25, 2019)

We study the phase diagram and the quantum phase transitions of a site-diluted two-dimensional O(3) quantum rotor model by means of large-scale Monte-Carlo simulations. This system has two quantum phase transitions, a generic one for small dilutions, and a percolation transition across the lattice percolation threshold. We determine the critical behavior for both transitions and for the multicritical point that separates them. In contrast to the exotic scaling scenarios found in other random quantum systems, all these transitions are characterized by finite-disorder fixed points with power-law scaling. We relate our findings to a recent classification of phase transitions with quenched disorder according to the rare region dimensionality, and we discuss experiments in disordered quantum magnets.

PACS numbers: 75.40.Mg, 75.10.Jm, 75.10.Nr

## I. INTRODUCTION

Quantum phase transitions occur at zero temperature when a nonthermal parameter like pressure, magnetic field, or chemical composition is varied. In the presence of defects, impurities, and other kinds of quenched disorder, the interplay between dynamic quantum fluctuations and static disorder fluctuations can lead to a variety of unconventional phenomena. Experimental examples include quantum Ising spin glasses,<sup>1,2</sup> heavy-fermion intermetallic compounds,<sup>3-6</sup> and other itinerant quantum magnets<sup>7</sup> as well as high-temperature superconductors,<sup>8,9</sup> the metal-insulator transition in metal-oxide-semiconductor field effect transistors (MOSFETs),<sup>10,11</sup> and superconductor-insulator transitions in thin films.<sup>12</sup>

Quenched disorder has interesting consequences already at classical phase transitions. In the early years, it was thought that impurities always destroy a critical point, because the system divides itself up into spatial regions that undergo the transition at different temperatures (see discussion in Ref. 13 and references therein). However, it soon became clear that in classical systems with short-range disorder correlations, the transition generically remains sharp. Harris<sup>14</sup> derived a criterion for the stability of a clean critical point against disorder: If the correlation length exponent  $\nu$  fulfills the inequality  $\nu > 2/d$ , where  $d$  is the spatial dimensionality, the critical behavior is not influenced by weak disorder. Harris' idea can be generalized to form the basis of a classification of critical points according to the behavior of the disorder strength under coarse graining.<sup>15</sup> The first class contains systems that fulfill the Harris criterion. In these systems, the disorder decreases without limit under coarse graining. The critical behavior is governed by a clean renormalization group fixed point, and macroscopic observables are self-averaging. In systems belonging to the second class, the disorder strength

approaches a nonzero constant for large length scales, corresponding to a fixed point with finite disorder. The critical behavior is thus different from that of the corresponding clean system, and macroscopic observables are not self-averaging.<sup>16,17</sup> Finally, the third class contains systems in which the disorder strength (counter-intuitively) *increases* without limit under coarse graining. The resulting infinite-randomness fixed point has unconventional properties including exponential rather than power-law scaling and very broad distributions of macroscopic observables.<sup>18,19</sup>

At zero-temperature quantum phase transitions, order-parameter fluctuations in space and time must be considered.<sup>20,21</sup> Quenched disorder is time-independent, it is thus perfectly correlated in one of the relevant dimensions, the (imaginary) time dimension. Because these correlations increase the effects of the disorder, quantum phase transitions are generically more strongly affected by disorder than classical transitions, potentially resulting in unconventional behavior. One of the earliest explicit examples was the random transverse-field Ising chain<sup>18,19,22</sup> (or the equivalent McCoy-Wu model<sup>23,24</sup>). This system belongs to the third of the classes discussed above, i.e., the critical point is of infinite-randomness type. The dynamical scaling is activated with the correlation time  $\xi_\tau$  and correlation length  $\xi$  being related by  $\ln \xi_\tau \sim \xi^\psi$ . (In contrast, at conventional critical points, this relation is a power law,  $\xi_\tau \sim \xi^z$ , with a universal dynamical exponent  $z$ ). Analogous behavior has been found, e.g., in the two-dimensional transverse-field Ising model<sup>15,25</sup> and in quantum Ising spin glasses.<sup>26,27</sup>

An important aspect of phase transitions in disordered systems are the so-called rare regions, large spatial regions that are devoid of impurities or more strongly coupled than the bulk system. These regions can be locally in the ordered phase even though the bulk system is still in the disordered phase. Griffiths<sup>28</sup> showed that this leads to a singularity (the Griffiths singularity) in the

free energy in an entire parameter region (the Griffiths region or Griffiths phase<sup>29</sup>) close to the phase transition. In generic classical systems with short-range disorder correlations, thermodynamic Griffiths effects are very weak because the singularity in the free energy is only an essential one. They are therefore probably unobservable in experiment. However, disorder correlations can greatly enhance the rare region effects.<sup>23,24</sup>

Since quenched disorder is perfectly correlated in the (imaginary) time direction, quantum phase transitions are expected to display stronger rare region effects than classical transitions. Indeed, in the above-mentioned random quantum Ising systems, the Griffiths singularities are of power-law type with the susceptibility diverging over a finite parameter range.<sup>18,19,22,26,27</sup> In itinerant quantum magnets, rare region effects can be even more dramatic. For Ising symmetry, the sharp quantum phase transition is destroyed by smearing<sup>30</sup> because sufficiently large rare regions stop tunneling. The same also happens in classical Ising magnets with plane defects<sup>31,32</sup> and at certain nonequilibrium phase transitions.<sup>33,34</sup> A recent review of these and other rare region effects can be found in Ref. 35.

In systems with continuous order parameter symmetry, the situation is more complex. The ground states of certain one-dimensional quantum spin chains are controlled by infinite-randomness fixed points.<sup>36</sup> On the other hand, in dimensions  $d \geq 2$ , the *stable low-energy* fixed point of random Heisenberg models has been shown to be conventional.<sup>37,38</sup> Preliminary renormalization group results<sup>15</sup> for the critical point in these models suggested that the infinite-randomness fixed point is unstable, implying more conventional behavior. This agrees with Monte-Carlo simulations of diluted single-layer<sup>39,40</sup> or bilayer<sup>41,42</sup> quantum Heisenberg antiferromagnets that did not show indications of exotic scaling. Note, however, that inhomogeneous bond disorder can induce a new quantum-disordered phase that can be understood as a quantum Griffiths phase.<sup>43</sup>

In this paper, we report the results of large-scale Monte-Carlo simulations of a diluted O(3) quantum rotor model in two space dimensions. We find that the system has two quantum phase transitions, a generic one for dilutions below the lattice percolation threshold  $p_c$  and a percolation type transition right at  $p_c$ . Both transitions and the multicritical point that separates them display conventional power-law critical behavior. For the generic transition, the critical exponents are universal, i.e., independent of the dilution. A short account of part of this work has already been published in Ref. 44. The present paper is organized as follows: In section II, we introduce the model and summarize the scaling theories for conventional and infinite-randomness critical points. The simulation method and our results for the phase diagram and the critical behavior of the quantum phase transitions are presented in section III. In the concluding section IV we relate our results to a general classification<sup>45</sup> of dirty phase transitions, and we consider experiments.

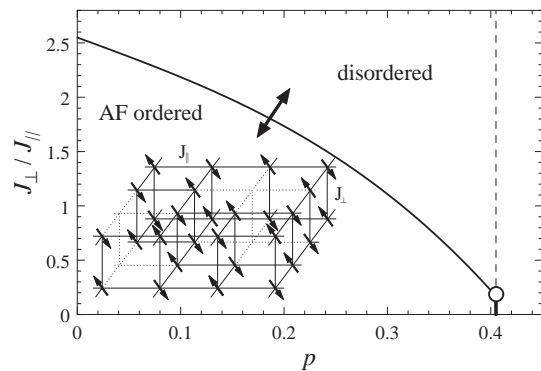


FIG. 1: Phase diagram of the diluted bilayer Heisenberg antiferromagnet, as function of  $J_{\perp}/J_{\parallel}$  and dilution  $p$ . The dashed line is the percolation threshold, the open dot is the multicritical point of Refs. 41,42. The arrow indicates the QPT studied here. Inset: The model: Quantum spins (arrows)  $\hat{\mathbf{S}}_{i,1}$  and  $\hat{\mathbf{S}}_{i,2}$  reside on the two parallel square lattices. The spins in each plane interact with the coupling strength  $J_{\parallel}$ . Inter-plane coupling is  $J_{\perp}$ . Dilution is done by removing dimers.

## II. THEORY

### A. Diluted quantum rotor model

We consider a site-diluted O(N) quantum rotor model defined on a square lattice. Its quantum Hamiltonian is given by<sup>21</sup>

$$\hat{H}_Q = U \sum_i \epsilon_i \hat{\mathbf{L}}_i^2 - J \sum_{\langle i,j \rangle} \epsilon_i \epsilon_j \hat{\mathbf{n}}_i \cdot \hat{\mathbf{n}}_j. \quad (1)$$

Here,  $\hat{\mathbf{n}}_i$  is an  $N$ -component unit vector at site  $i$ . Conjugate momenta  $\hat{\mathbf{p}}_i$  are defined via the usual canonical commutation relations  $[\hat{n}_i^\alpha, \hat{p}_i^\beta] = i\delta_{\alpha\beta}$  on each site  $i$ . ( $\alpha, \beta = 1 \dots N$  are the component indices, and we work in units in which  $\hbar = 1$ .) The components of the angular momentum  $\hat{\mathbf{L}}$  of each rotor are given by  $\hat{L}^{\alpha\beta} = \hat{n}_i^\alpha \hat{p}_i^\beta - \hat{n}_i^\beta \hat{p}_i^\alpha$ . The site dilution is described by the independent random variable  $\epsilon_i$  which can take the value 0 and 1 with probability  $p$  and  $1-p$ , respectively.

Elementary quantum rotors do not exist in nature; rather, they arise as effective low-energy degrees of freedom of correlated quantum systems. For example, O(2) quantum rotor models describe superconducting Josephson junction arrays or bosons in optical lattices. An  $N=3$  quantum rotor describes the states of an even number of antiferromagnetically coupled Heisenberg spins. A specific example is provided by the bilayer quantum Heisenberg antiferromagnet depicted in the inset of Fig. 1. This system is equivalent to an O(3) quantum rotor model with each dimer ( $\hat{\mathbf{S}}_{i,1}, \hat{\mathbf{S}}_{i,2}$ ) of spins at site  $i$  and layers 1 and 2 being represented by a single rotor. The rotor coordinate  $\hat{\mathbf{n}}_i$  corresponds to  $\hat{\mathbf{S}}_{i,1} - \hat{\mathbf{S}}_{i,2}$  and the angular momentum  $\hat{\mathbf{L}}_i$  corresponds to  $\hat{\mathbf{S}}_{i,1} + \hat{\mathbf{S}}_{i,2}$  (see, e.g., chapter 5 of Ref. 21). The O(3) quantum rotors also describe

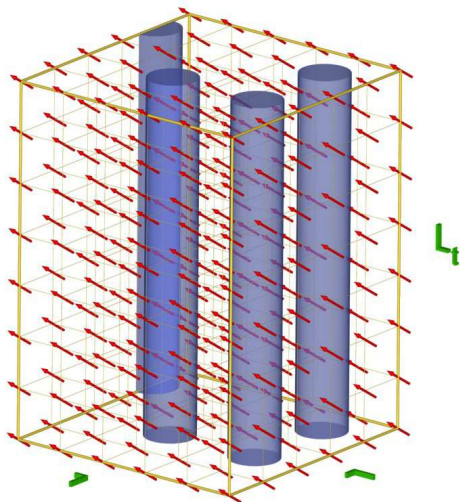


FIG. 2: Sketch of the classical model (2). The arrows represent the classical spins and the tubes show the locations of the linear defects (vacancies).

double-layer quantum Hall ferromagnets.

We now focus on the  $O(3)$  site-diluted quantum rotor model on a square lattice. Since we will be mostly interested in the universal critical behavior, we now map the quantum system onto a classical system in the same universality class. This can be easily achieved via a path integral representation of the partition function.<sup>21</sup> The resulting classical system is a three-dimensional Heisenberg model with the extra dimension representing the imaginary time coordinate of the quantum rotor model. Because the impurities in the quantum rotor model are quenched (i.e., time-independent), the defects in the classical system are linear, i.e., the disorder is perfectly correlated in the extra (imaginary time) direction (see Fig. 2). Thus, our classical Hamiltonian reads:

$$H = K \sum_{\langle i,j \rangle, \tau} \epsilon_i \epsilon_j \mathbf{n}_{i,\tau} \cdot \mathbf{n}_{j,\tau} + K \sum_{i,\tau} \epsilon_i \mathbf{n}_{i,\tau} \cdot \mathbf{n}_{i,\tau+1}, \quad (2)$$

where  $\mathbf{n}_{i,\tau}$  is an  $O(3)$  unit vector at the lattice site with spatial coordinate  $i$  and “imaginary time” coordinate  $\tau$ . The coupling constant  $\beta K$  of the classical model is related to the ratio  $U/J$  of the quantum rotor model. Here,  $\beta \equiv 1/T$  where  $T$  is an effective “classical” temperature, not equal to the real temperature in the quantum model which is zero. We set  $K = 1$  and drive the classical system through the transition by tuning the classical temperature  $T$ .

As an aside, we note that in the above-mentioned bilayer Heisenberg antiferromagnet the dilution has to be done by removing dimers of corresponding spins in the two layers because each dimer is described by a single rotor. In contrast, for site dilution, the physics changes completely: Random Berry phase terms with no classical analogue arise. They are equivalent to impurity-induced moments,<sup>46</sup> and those become weakly coupled via bulk

excitations. Thus, for all dilutions below the percolation threshold,  $p < p_c$ , the ground state shows long-range order, independent of the coupling constants! This effect is absent for dimer dilution, and both phases of the clean system survive for small dilution.

## B. Power-law vs. activated scaling

In this subsection, we summarize the conventional and activated scaling scenarios at critical points with quenched disorder to the extent necessary for the analysis of our simulation results.

At conventional (quantum) critical points, correlation length  $\xi$  and correlation time  $\xi_\tau$  are related by a power-law,  $\xi_\tau \propto \xi^z$  with  $z$  being the dynamical critical exponent. (Note that in the effective classical system (2),  $\xi$  and  $\xi_\tau$  are the correlation lengths in the space-like and time-like directions, respectively.) This is referred to as power-law dynamical scaling. In contrast, at infinite-randomness critical points, the dynamical scaling is activated, i.e., the relation between correlation length and time is exponential,  $\ln(\xi_\tau) \propto \xi^\psi$ .<sup>18,19</sup>

These differences in the dynamical scaling lead to analogous differences in the finite-size scaling behavior of observables. If we denote the linear system size in the two space-like dimensions by  $L$  and the size in the time-like dimension by  $L_\tau$ , the finite-size scaling forms of the magnetization per site  $m = |\mathbf{m}|$  and the susceptibility  $\chi$  at a conventional critical point read

$$m = L^{-\beta/\nu} \tilde{m}_C(tL^{1/\nu}, L_\tau/L^z), \quad (3)$$

$$\chi = L^{\gamma/\nu} \tilde{\chi}_C(tL^{1/\nu}, L_\tau/L^z). \quad (4)$$

Here,  $t$  is the dimensionless distance from the critical point; and  $\beta, \gamma$  and  $\nu$  are the critical exponents of magnetization, susceptibility, and correlation length, respectively. At an infinite-randomness critical point, the scaling combination  $L_\tau/L^z$  has to be replaced by  $\ln(L_\tau)/L^\psi$  leading to the finite-size scaling forms

$$m = L^{-\beta/\nu} \tilde{m}_A(tL^{1/\nu}, \ln(L_\tau)/L^\psi), \quad (5)$$

$$\chi = L^{\gamma/\nu} \tilde{\chi}_A(tL^{1/\nu}, \ln(L_\tau)/L^\psi). \quad (6)$$

In addition to magnetization and susceptibility we also calculate three quantities whose scale dimension is zero which makes them particularly suitable for locating the critical point and extracting high precision values for the correlation length and dynamical exponents. The first such quantity is the Binder ratio. It is defined by

$$g_{av} = \left[ 1 - \frac{\langle |\mathbf{m}|^4 \rangle}{3 \langle |\mathbf{m}|^2 \rangle^2} \right]_{av}, \quad (7)$$

where  $[\dots]_{av}$  denotes the disorder average and  $\langle \dots \rangle$  denotes the Monte-Carlo average for each sample. This quantity approaches well-known limits in both bulk phases (stable fixed points): In the ordered phase, all

spins are correlated, and the magnetization has small fluctuations around a nonzero value. Therefore,  $\langle |\mathbf{m}|^4 \rangle \approx \langle |\mathbf{m}|^2 \rangle^2$ , and the Binder ratio approaches  $2/3$ . In the disordered phase, the system consists of many independent fluctuators. Consequently,  $\langle |\mathbf{m}|^4 \rangle$  can be decomposed using Wick's theorem. For  $O(3)$  symmetry this gives  $\langle |\mathbf{m}|^4 \rangle \approx (15/9) \langle |\mathbf{m}|^2 \rangle^2$ , and the Binder ratio approaches  $4/9$ . More generally, the Binder ratio is large if all spins are correlated and decreases if the system contains independently fluctuation units. Because the Binder ratio has scale dimension zero, its finite-size scaling form is given by

$$g_{av} = \tilde{g}_C(tL^{1/\nu}, L_\tau/L^z) \quad \text{or} \quad (8)$$

$$g_{av} = \tilde{g}_A(tL^{1/\nu}, \ln(L_\tau)/L^\psi) \quad (9)$$

for conventional scaling or for activated scaling, respectively. Two important characteristics follow from the scaling form and the discussion above:<sup>47,48</sup> (i) For fixed  $L$ ,  $g_{av}$  has a peak as a function of  $L_\tau$ . The peak position  $L_\tau^{\max}$  marks the *optimal* sample shape, where the ratio  $L_\tau/L$  roughly behaves like the corresponding ratio of the correlation lengths in time and space directions,  $\xi_\tau/\xi$ . (If the aspect ratio deviates from the optimal one, the system can be decomposed into independent units either in space or in time direction, and thus  $g_{av}$  decreases.) At the critical temperature  $T_c$ , the peak value  $g_{av}^{\max}$  is independent of  $L$ . Thus, for power law scaling, plotting  $g_{av}$  vs.  $L_\tau/L_\tau^{\max}$  at  $T_c$  should collapse the data, without the need for a value of  $z$ . In contrast, for activated scaling the  $g_{av}$  data should collapse when plotted as a function of  $\log(L_\tau)/\log(L_\tau^{\max})$ . (ii) For samples of the optimal shape ( $L_\tau = L_\tau^{\max}$ ), plots of  $g_{av}$  vs. temperature for different  $L$  cross at  $T_c$ .

The other two quantities of scale dimension zero we consider, are the ratios of disconnected correlation lengths and system sizes in both space and time-like dimensions. Here, the disconnected correlation lengths  $\xi^{dis}$  and  $\xi_\tau^{dis}$  arise from the disconnected correlation function  $\langle \mathbf{n}_{i,\tau} \mathbf{n}_{j,\tau'} \rangle$ . In contrast the usual, connected correlation lengths  $\xi$  and  $\xi_\tau$  arise from the connected correlation function  $\langle \mathbf{n}_{i,\tau} \mathbf{n}_{j,\tau'} \rangle - \langle \mathbf{n}_{i,\tau} \rangle \langle \mathbf{n}_{j,\tau'} \rangle$ . The finite-size scaling forms of our ratios for conventional and activated scaling read

$$\xi^{dis}/L = X_C(tL^{1/\nu}, L_\tau/L^z) \quad \text{or} \quad (10)$$

$$\xi^{dis}/L = X_A(tL^{1/\nu}, \ln(L_\tau)/L^\psi), \quad (11)$$

and

$$\xi_\tau^{dis}/L_\tau = Y_C(tL^{1/\nu}, L_\tau/L^z) \quad \text{or} \quad (12)$$

$$\xi_\tau^{dis}/L_\tau = Y_A(tL^{1/\nu}, \ln(L_\tau)/L^\psi), \quad (13)$$

respectively. Calculating these quantities provides independent checks for the location of the critical point and for the exponents  $z$  (or  $\psi$ ) and  $\nu$ .

### III. SIMULATIONS

#### A. Monte Carlo method

In order to study the phase transitions of the effective classical model (2) we perform large scale Monte-Carlo simulations. We use the efficient Wolff cluster algorithm<sup>49</sup> to reduce the effects of the critical slowing down close to the phase transition. This is possible because the dilution-disorder does not introduce frustration, and all interactions are ferromagnetic. We investigate linear sizes up to  $L = 120$  in space direction and  $L_\tau = 2560$  in imaginary time direction, for impurity concentrations  $p = \frac{1}{8}, \frac{1}{5}, \frac{2}{7}, \frac{1}{3}$  and  $p_c = 0.407253$  which is the lattice percolation threshold. For the larger dilutions,  $p = \frac{2}{7}, \frac{1}{3}$ , and  $p_c$  we perform both Wolff and Metropolis sweeps to equilibrate small dangling clusters.

The determination of averages, variances, and distribution functions of observables in disordered systems requires the simulation of many independent samples with different impurity configurations. Because of the huge computational effort involved,<sup>50</sup> one must carefully choose the number  $N_S$  of disorder realizations (i.e., samples) and the number  $N_I$  of measurements during the simulation of each sample for optimal performance. Assuming full statistical independence between different measurements (quite possible with a cluster update), the variance  $\sigma_T^2$  of the final result (thermodynamically and disorder averaged) for a particular observable is given by<sup>51,52</sup>

$$\sigma_T^2 = (\sigma_S^2 + \sigma_I^2/N_I)/N_S \quad (14)$$

where  $\sigma_S$  is the disorder-induced variance between samples and  $\sigma_I$  is the variance of measurements within each sample. Since the computational effort is roughly proportional to  $N_I N_S$  (neglecting equilibration for the moment), it is then clear that the optimum value of  $N_I$  is very small. One might even be tempted to measure only once per sample. On the other hand, with too short measurement runs most computer time would be spent on equilibration.

In order to balance these requirements we have used a large number  $N_S$  of disorder realizations, ranging from 1000 to several 10000, depending on the system size and rather short runs of 100-200 Monte-Carlo sweeps, with measurements taken after every sweep. (A sweep is defined by a number of cluster flips so that the total number of flipped spins is equal to the number of sites, i.e., on the average each spin is flipped once per sweep.) The length of the equilibration period for each sample is also 100 Monte-Carlo sweeps. The actual equilibration times have typically been of the order of 10-20 sweeps at maximum. Thus, an equilibration period of 100 sweeps should be more than sufficient.

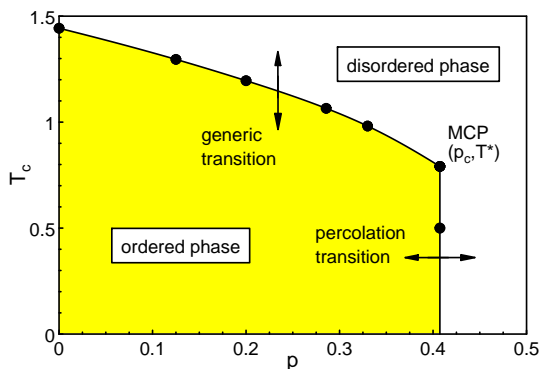


FIG. 3: Phase diagram of the three-dimensional Heisenberg model (2) as function of temperature  $T$  and concentration  $p$  of linear defects. MCP is the multicritical point. The big dots mark the numerically determined transition points. The lines are guides for the eye.

### B. Results: phase diagram

We start the discussion of our results by considering the phase diagram of the classical Hamiltonian (2) in the dilution-temperature plane. To determine the critical temperature  $T_c$  for a given dilution  $p$ , we use a simple iterative procedure based on the properties of the Binder ratio  $g_{av}$  discussed after (9). We start with a guess for the dynamical exponent  $z$  (or, alternatively  $\psi$  for activated scaling). We then perform a number of simulation runs to calculate  $g_{av}$  as a function of temperature for samples whose linear sizes fulfill  $L_\tau \propto L^z$ . The approximate crossing of the  $g_{av}$  vs.  $T$  curves for different  $L$  gives an estimate for  $T_c$ . At this temperature, we now calculate  $g_{av}$  as a function of  $L_\tau$  for fixed  $L$ . The maxima of these curves give an improved estimate for the “optimal shapes”, i.e., for the dynamical exponent  $z$ . This procedure can be repeated until the estimate for  $T_c$  converges. Typically, only two to three iterations were necessary for the desired accuracy.

The resulting phase diagram is shown in Fig. 3. As expected,  $T_c(p)$  decreases with increasing dilution  $p$ , but the ordered phase survives up to the lattice percolation threshold  $p_c$  with  $T^* = T_c(p_c) > 0$ . Thus, the classical Heisenberg model (2) with linear defects has two phase transitions, viz., a generic transition for  $p < p_c$  and a percolation type transition for  $p = p_c$  and  $T < T^*$ . They are separated by a multicritical point at  $(p_c, T^*)$ . Analogous behavior was found in the dimer-diluted bilayer quantum Heisenberg antiferromagnet<sup>41,42</sup> (see also Fig. 1).

We have carried out detailed investigations of both transitions and of the multicritical point. Our results for the critical behaviors will be presented in the next three subsections.

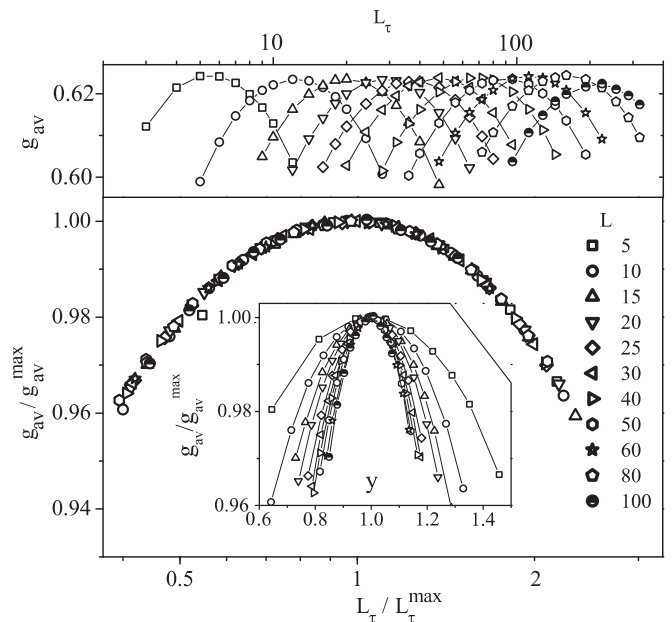


FIG. 4: Upper panel: Binder ratio  $g_{av}$  as a function of  $L_\tau$  for various  $L$  ( $p = \frac{1}{5}$ ). Lower panel: Power-law scaling plot  $g_{av}/g_{av}^{max}$  vs.  $L_\tau/L_\tau^{max}$ . Inset: Activated scaling plot  $g_{av}/g_{av}^{max}$  vs.  $y = \log(L_\tau)/\log(L_\tau^{max})$ .

### C. Generic critical point for $p < p_c$

To determine the critical behavior of the generic transitions and to test its universality, we have considered four different impurity concentrations,  $p = \frac{1}{8}, \frac{1}{5}, \frac{2}{7}$ , and  $\frac{1}{3}$ . For each concentration we have performed two types of simulations: The first consists of runs right at  $T_c(p)$  for systems of different sizes  $L$  and  $L_\tau$  with varying aspect ratio  $L_\tau/L$ . The finite-size scaling properties of  $g_{av}$ ,  $m$ , and  $\chi$  allow us to extract the dynamical exponent  $z$ , as well as  $\beta/\nu$  and  $\gamma/\nu$ . In the second set of simulations, we vary the temperature over a range in the vicinity of  $T_c$ , but we consider only samples of “optimal shape”,  $L_\tau \propto L^z$ , using the value of  $z$  found in the first part. Finite-size scaling then yields the correlation length exponent  $\nu$ .

Let us start by discussing the behavior of the Binder ratio  $g_{av}$  right at the critical temperature  $T_c(p)$ . The upper panel of Fig. 4 shows  $g_{av}$  as a function of  $L_\tau$  for various  $L = 5$  to 100 and dilution  $p = \frac{1}{5}$  at  $T = T_c = 1.1955$ . The statistical error of  $g_{av}$  is below 0.1% for the smaller sizes and not more than 0.2% for the largest systems. As expected at  $T_c$ , the maximum Binder ratio for each of the curves does not depend on  $L$ . We now discriminate between power-law dynamical scaling (8) and activated dynamical scaling (9). To this end, we plot  $g_{av}/g_{av}^{max}$  as a function of  $L_\tau/L_\tau^{max}$  in the lower panel of Fig. 4. The data scale extremely well, giving statistical errors of  $L_\tau^{max}$  in the range between 0.3% and 1%. For comparison, the inset shows a plot of  $g_{av}$  as a function of  $\log(L_\tau)/\log(L_\tau^{max})$  corresponding to activated dynamical

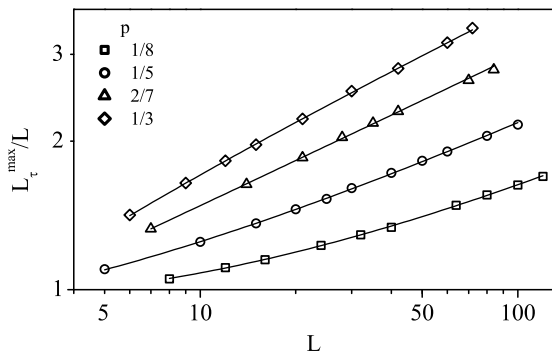


FIG. 5:  $L_\tau^{max}/L$  vs.  $L$  for dilutions  $p = \frac{1}{8}, \frac{1}{5}, \frac{2}{7}$  and  $\frac{1}{3}$ . Solid lines: Fit to  $L_\tau^{max} = aL^z(1 + bL^{-\omega_1})$  with  $z = 1.310(6)$  and  $\omega_1 = 0.48(3)$ .

cal scaling (9). Plotted this way, the data clearly do not scale. The results for the other impurity concentrations  $p = \frac{1}{8}, \frac{2}{7}, \frac{1}{3}$  are completely analogous.

This analysis establishes that the dynamical scaling at the generic transition is of conventional power-law type. We now proceed to determine the dynamical exponent  $z$  and to study whether or not it is universal, i.e., independent of the dilution  $p$ . According to (8), the maximum positions  $L_\tau^{max}$  should depend on  $L$  via a power law with the exponent  $z$ . In Fig. 5, we plot  $L_\tau^{max}$  vs.  $L$  for all four dilutions  $p$ . The curves show significant deviations from pure power-law behavior which can be attributed to corrections to scaling due to irrelevant operators. In such a situation, a direct power-law fit of the data will only yield *effective* exponents. To find the true *asymptotic* exponents we take the leading correction to scaling into account by using the ansatz  $L_\tau^{max}(L) = aL^z(1 + bL^{-\omega_1})$  with universal (dilution-independent) exponents  $z$  and  $\omega_1$  but dilution-dependent  $a$  and  $b$ . A combined fit of all four curves gives  $z = 1.310(6)$  and  $\omega_1 = 0.48(3)$  where the number in brackets is the *statistical* error of the last given digit. The fit is of high quality ( $\chi^2 \approx 0.7$ ) and robust against removing complete data sets or removing points from the lower or upper end of each set. We thus conclude that the asymptotic dynamical exponent  $z$  is indeed universal. Note that the leading corrections to scaling vanish very close to  $p = \frac{2}{7}$ ; the curvature of the  $L_\tau^{max}(L)$  curves in Fig. 5 is opposite above and below this concentration. A straight power-law fit of the  $L_\tau^{max}$  vs.  $L$  curve for this dilution gives  $z = 1.303(3)$  in good agreement with the value from the global fit.

We now turn to the exponents  $\beta/\nu$  and  $\gamma/\nu$ . According to eqs. (3) and (4), they can be obtained from the  $L$ -dependence of the magnetization and susceptibility at  $T_c$  of the optimally shaped samples ( $L_\tau = L_\tau^{max}$ ). In Fig. 6 we plot the magnetization data for all four dilutions  $p = \frac{1}{8}, \frac{1}{5}, \frac{2}{7}$ , and  $\frac{1}{3}$ . The plots do not show strong curvature, and straight power-law fits give values between 0.495 and 0.568 for the exponent  $\beta/\nu$ . This could be taken as an indication for nonuniversal behavior. However, given that  $z$  is universal, we have also attempted a combined fit

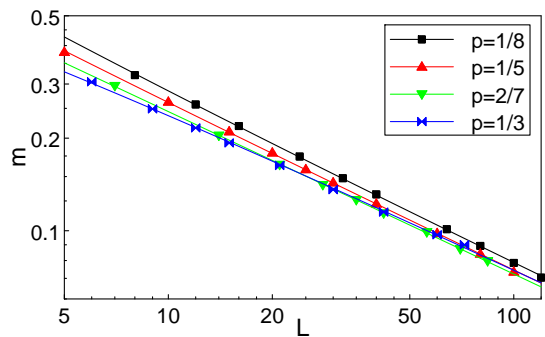


FIG. 6:  $m$  vs.  $L$  at  $T_c$  for optimally shaped samples at dilutions  $p = \frac{1}{8}, \frac{1}{5}, \frac{2}{7}$  and  $\frac{1}{3}$ . Solid lines: Fit to  $m = aL^{-\beta/\nu}(1 + bL^{-\omega_1})$  with  $\beta/\nu = 0.53(3)$  and  $\omega_1 = 0.48$ .

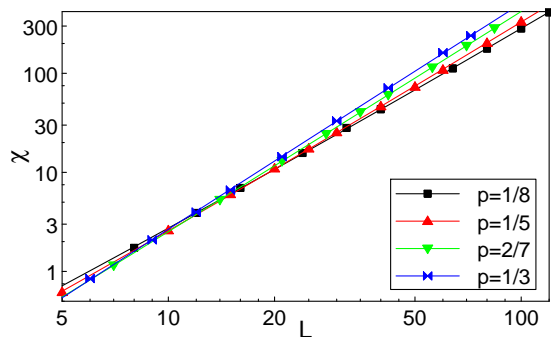


FIG. 7:  $\chi$  vs.  $L$  at  $T_c$  for optimally shaped samples at dilutions  $p = \frac{1}{8}, \frac{1}{5}, \frac{2}{7}$  and  $\frac{1}{3}$ . Solid lines: Fit to  $\chi = aL^{\gamma/\nu}(1 + bL^{-\omega_1})$  with  $\gamma/\nu = 2.26(6)$  and  $\omega_1 = 0.48$ .

of all four curves to  $m(L) = cL^{-\beta/\nu}(1 + dL^{-\omega})$  with universal  $\beta/\nu$  and  $\omega$  (fixed to the value  $\omega_1 = 0.48^{62}$ ) but dilution-dependent  $c$  and  $d$ . The combined fit works well ( $\chi^2 \approx 1.6$ ) and gives an asymptotic exponent of  $\beta/\nu = 0.53(3)$ . For comparison, a straight power-law fit for  $p = \frac{2}{7}$  (which is the dilution where the corrections to scaling approximately vanish, see above) gives  $\beta/\nu = 0.527$  in good agreement with the value from the global fit. We thus conclude that the data display no indication of a nonuniversal  $\beta/\nu$ .

The analogous plot for the susceptibility data is shown in Fig. 7. Straight power law fits give effective values between 2.02 and 2.28 for  $\gamma/\nu$ . The combined fit of all four curves to the ansatz  $m(L) = eL^{\gamma/\nu}(1 + fL^{-\omega})$  with  $\omega = 0.48$  gives a universal asymptotic exponent  $\gamma/\nu = 2.26(6)$ . Again, a straight power-law fit to the data for  $p = \frac{2}{7}$  gives a value (viz.,  $\gamma/\nu = 2.22$ ) in good agreement with the global fit.

The exponents  $\beta/\nu$ ,  $\gamma/\nu$  and  $z$  are not all independent from each other; they must fulfill the hyperscaling relation  $2\beta/\nu + \gamma/\nu = d + z$ . Our values  $\beta/\nu = 0.53(3)$ ,  $\gamma/\nu = 2.26(6)$ , and  $z = 1.310(6)$  fulfill the hyperscaling relation within the error bars, indicating that they can indeed be asymptotic values rather than effective exponents.

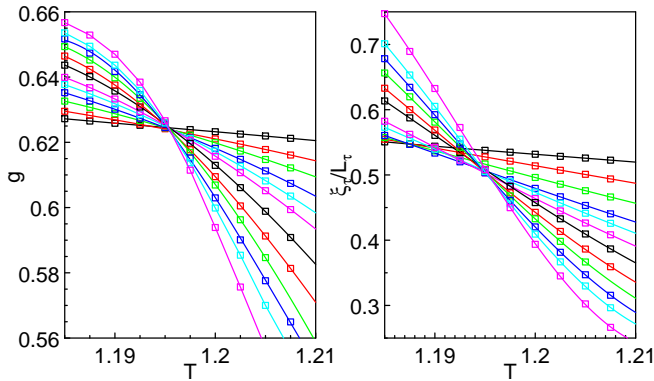


FIG. 8: Binder ratio  $g_{av}$  (left) and  $\xi_\tau^{dis}/L_\tau$  (right) as functions of temperature  $T$  for dilution  $p = 0.2$ . System sizes range from  $L = 5$  to  $L = 100$  with increasing slope.

After having discussed the simulations right at  $T_c$ , we now vary the temperature over a range in the vicinity of  $T_c$ , but we consider only samples of “optimal shape”  $L_\tau = L_\tau^{max}$  to keep the second argument of the scaling functions in eqs. (3), (4), (8), (10), and (12) constant. Fig. 8 shows the Binder ratio  $g_{av}$  and the ratio  $\xi_\tau^{dis}/L_\tau$  as functions of temperature for various  $L = 5$  to 100 and dilution  $p = \frac{1}{5}$ . (The correlation lengths have been calculated in the usual way via the lowest Fourier components of the spin-spin correlation function.<sup>53,54</sup>) The Binder ratio shows a near perfect crossing point, i.e., the corrections to scaling for this quantity are very small. In contrast,  $\xi_\tau^{dis}/L_\tau$  displays larger corrections to scaling indicated by the drift of the the crossing point between different  $\xi_\tau^{dis}/L_\tau$  curves with  $L$ . The behavior of  $\xi_\tau^{dis}/L$  (not shown) is very similar to that of  $\xi_\tau^{dis}/L_\tau$ .

We have therefore used a scaling analysis of the Binder cumulant as our main tool for determining  $\nu$ . Fig. 9 shows a scaling plot of  $g_{av}$  vs.  $x_L T$  for impurity concentration  $p = \frac{1}{5}$ . (Here  $x_L$  is the scaling factor necessary to collapse the data onto a master curve.) The quality of the scaling is very good, comparable to that in Fig. 4. However, since the scaling function lacks the characteristic maximum, the error of the resulting scaling factor  $x_L$  is somewhat larger (1 to 2%) than that of  $L_\tau^{max}$ . The data for other dilutions  $p = \frac{1}{8}, \frac{2}{7}$  and  $\frac{1}{3}$  lead to analogous scaling plots. To determine the correlation length exponent  $\nu$ , we plot the scaling factor  $x_L$  vs.  $L$  for all four dilutions in Fig. 10. Similar to the  $L_\tau^{max}$  vs.  $L$  curves in Fig. 4, the  $x_L$  vs.  $L$  curves show significant curvatures necessitating an ansatz  $x_L = cL^{1/\nu}(1 + dL^{-\omega_2})$  that includes corrections to scaling. A combined fit of all four curves to this ansatz (with universal  $\nu$  and  $\omega_2$ ) gives  $\nu = 1.16(3)$  and  $\omega_2 = 0.5(1)$ . As above, the fit is robust and of high quality ( $\chi^2 \approx 1.2$ ). Importantly, as expected for the true asymptotic exponent,  $\nu$  fulfills the Harris criterion,<sup>14</sup>  $\nu > 2/d=1$ . Note that both irrelevant exponents  $\omega_1$  and  $\omega_2$  agree within their error bars, suggesting that the same irrelevant operator controls the

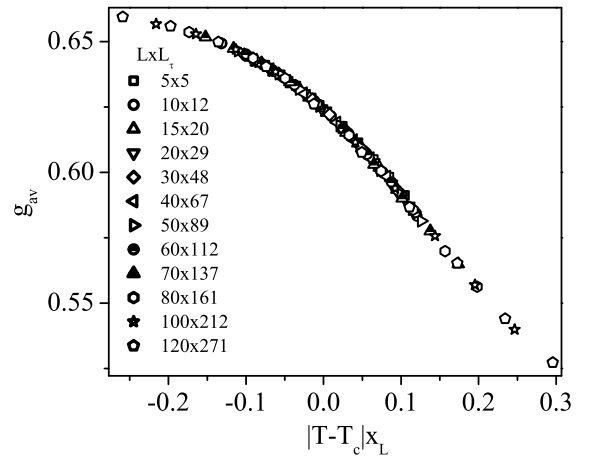


FIG. 9: Scaling plot of  $g_{av}$  vs.  $(T - T_c)x_L$  for  $p = 0.2$ .  $x_L$  is the factor necessary to scale the data onto a master curve.

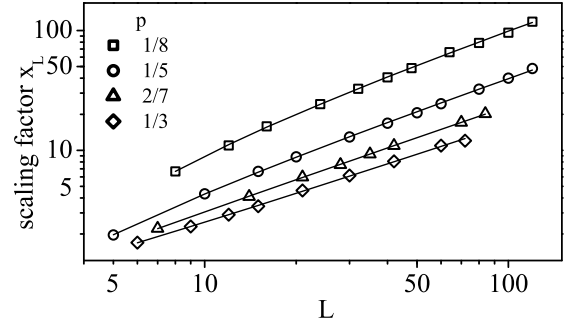


FIG. 10: Scaling factor vs.  $L$  for four disorder concentrations  $p = \frac{1}{8}, \frac{1}{5}, \frac{2}{7}$  and  $\frac{1}{3}$ . Solid lines: Fit to  $x_L = gL^{1/\nu}(1 + hL^{-\omega_2})$  with  $\nu = 1.16(3)$  and  $\omega_2 = 0.5(1)$ .

leading corrections to scaling for both  $z$  and  $\nu$ . For comparison, we have also performed a straight power-law fit for the dilution where the corrections to scaling approximately vanish,  $p = \frac{2}{7}$ . It gives  $\nu = 1.12(3)$  in agreement with the value from the global fit.

We have also performed an analogous scaling analysis of  $\xi_\tau/L_\tau$ . Because of the larger corrections to scaling, the errors of the scale factors (i.e., slopes of the curves) are significantly higher, but within the error bar, the value of  $\nu$  agrees with that determined from  $g_{av}$ .

#### D. Percolation transition at $p = p_c$

After having discussed the generic dirty quantum rotor phase transition realized for  $p < p_c$ , we now turn to the percolation-type transition occurring for  $p = p_c$  and  $T < T^*$ . At this transition, the dynamical fluctuations of the rotors are noncritical; and the critical behavior is due to the critical geometry of the percolating lattice. Vojta and Schmalian<sup>55</sup> have developed a complete scaling theory for this percolation quantum phase transition. They have also calculated exact exponent values for the case of two

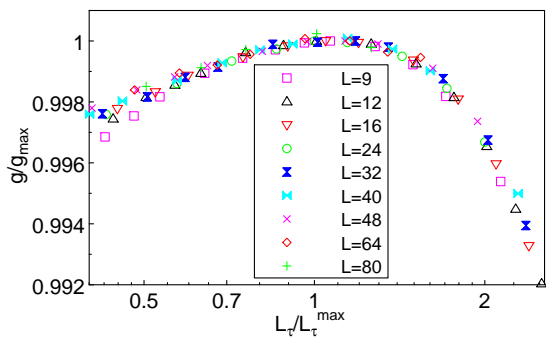


FIG. 11: Power-law scaling plot  $g_{av}/g_{av}^{max}$  vs.  $L_\tau/L_\tau^{max}$  for  $p = p_c = 0.407253$  and  $T = 0.5$ .

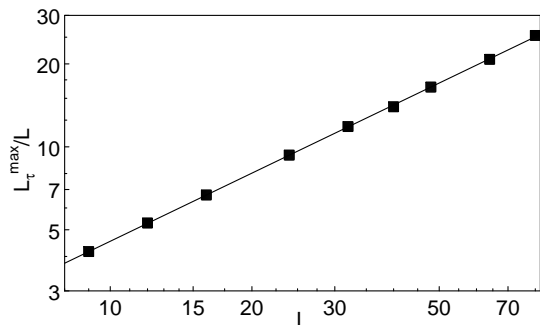


FIG. 12:  $L_\tau^{max}/L$  vs.  $L$  for dilution  $p = p_c = 0.407253$  and  $T = 0.5$ . Solid line: Power-law fit giving  $z = 1.83(3)$ .

space dimensions, viz.,  $z = 91/48$ ,  $\nu = 4/3$ ,  $\beta = 5/36$ , and  $\gamma = 59/12$ .

In this subsection, we test these theoretical predictions by performing simulations at  $p = p_c = 0.407253$  and  $T = 0.5$ . For two reasons, these calculations require significantly higher numerical effort than those in the last subsection: (i) Due to the large value of the dynamical exponent  $z$ , the “optimal” linear size  $L_\tau^{max}$  in the time-like direction increases very rapidly with  $L$ . For our largest  $L = 80$ , the optimal  $L_\tau$  turns out to be  $L_\tau^{max} = 2030$  leading to a system of 13 million spins. (ii) The very strong geometric fluctuations of the lattice at the percolation threshold lead to noisier data. Thus a larger number of disorder realizations has to be averaged.

Figure 11 shows the resulting scaling plot for the Binder cumulant as a function of  $L_\tau/L_\tau^{max}$  for systems of sizes  $L = 9$  to 80. The data scale reasonably well, but the quality is clearly less than that of the corresponding plot for the generic transition (Fig. 4). Moreover there seems to be a small systematic broadening of the domes with increasing  $L$  which is likely caused by finite-size corrections to the critical lattice percolation problem. The resulting values of  $L_\tau^{max}$  have statistical errors of about 5%. To determine the dynamical exponent  $z$ , we plot  $L_\tau^{max}$  vs.  $L$  in Fig. 12. The data can be well fitted by a power law giving an exponent of  $z = 1.83(3)$ . The remaining small difference to the theoretical value  $91/48 \approx 1.89$

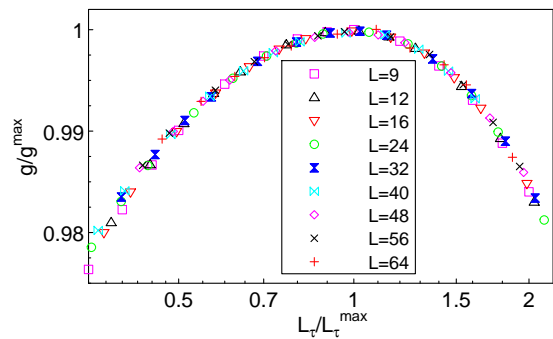


FIG. 13: Power-law scaling plot  $g_{av}/g_{av}^{max}$  vs.  $L_\tau/L_\tau^{max}$  for the multicritical point at  $p = p_c = 0.407253$  and  $T = T^* = 0.791$ .

can probably be attributed to corrections scaling for our rather small  $L$ . Indeed, a fit of the  $L_\tau^{max}$  vs.  $L$  data to the ansatz  $L_\tau^{max}(L) = aL^{91/48}(1 + bL^{-\omega})$  is almost indistinguishable from the power-law fit.

In addition to the Binder ratio we have also analyzed magnetization  $m$  and susceptibility  $\chi$  for the optimally shaped samples ( $L_\tau = L_\tau^{max}$ ). In analogy to Figs. 6 and 7, the  $L$ -dependencies of  $m$  and  $\chi$  give the exponents  $\beta/\nu$  and  $\gamma/\nu$ , respectively. The  $m$  vs.  $L$  curve shows noticeable upward curvature; and while a power-law fit gives  $\beta/\nu = 0.15(3)$ , using the ansatz  $m(L) = cL^{5/48}(1 + dL^{-\omega})$  actually leads to a significantly better fit (lower  $\chi^2$ ). For the susceptibility, a power-law fit of the  $\chi$  vs.  $L$  data gives  $\gamma/\nu = 3.51(5)$  which is somewhat smaller than the theoretical value of  $59/16 \approx 3.68$ . However, a fit to the ansatz  $\chi(L) = eL^{59/16}(1 + fL^{-\omega})$  is of comparable quality.

## E. Multicritical point

In this last subsection on results, we consider the multicritical point  $(p_c, T^*)$  that separates the generic transition from the percolation transition. In contrast to the percolation transition, no quantitative theoretical predictions are available for the multicritical point. We have performed simulations at  $p = p_c = 0.407253$  and  $T = T^* = 0.791$  for  $L = 9$  to 64. Because of the simultaneous presence of critical geometric and dynamical fluctuations, the necessary number of disorder realizations is even larger than for the percolation transition. We have used between 10000 and 50000 realizations, depending on system size.

Figure 13 shows the resulting scaling plot for the Binder cumulant as a function of  $L_\tau/L_\tau^{max}$ . The data scale very well, giving statistical errors for  $L_\tau^{max}$  of approximately 2%. Note that the data show a very slight systematic broadening of the domes with increasing  $L$ . It is much weaker than for the percolation transition at  $T = 0.50$  (Fig. 11), but probably, it can also be attributed to finite-size corrections to the critical lattice percolation



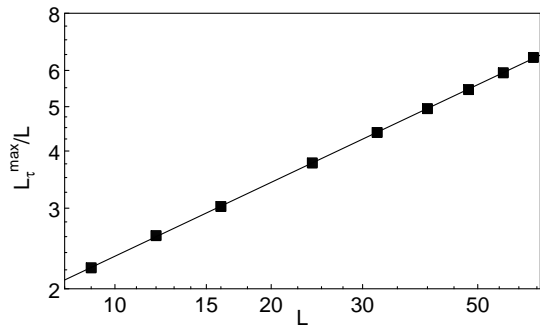


FIG. 14:  $L_t^{max}/L$  vs.  $L$  for the multicritical point  $p = p_c = 0.407253$  and  $T = T^* = 0.791$ . Solid line: Power-law fit giving  $z = 1.54(2)$ .

problem. Fig. 14 shows a log-log plot of  $L_t^{max}$  vs  $L$ . The curve does not show a discernable deviation from a straight line, and a power-law fit gives  $z = 1.54(2)$ . Given the fact that the same analysis gave a very slightly too small  $z$ -value at the percolation transition, the true asymptotic exponent may be a few percent higher than the fit result. We have also determined the exponents  $\beta/\nu$  and  $\gamma/\nu$  from the  $L$ -dependencies of the magnetization and susceptibility for the optimally shaped samples. As at the percolation transition, the  $m(L)$  curve shows some upward curvature; and while a power-law fit gives  $\beta/\nu = 0.40(3)$ , the true asymptotic exponent may be a bit lower. Unfortunately, our  $L$ -range is not wide enough for a stable fit to an ansatz that includes corrections to scaling (and thus has two unknown exponents and two prefactors). In contrast, the  $\chi(L)$  curve does not show any deviations from power-law behavior, and a fit gives  $\gamma/\nu = 2.71(3)$ . Again, from the analogy with the percolation transition, the true asymptotic exponent may be slightly higher.

#### IV. CONCLUSIONS

We have investigated the quantum phase transitions of a two-dimensional site-diluted  $O(3)$  rotor model by performing large-scale Monte-Carlo simulations of the equivalent classical model, a three-dimensional classical Heisenberg model with linear defects. In this final section we summarize the results and relate them to a recent classification<sup>35,45</sup> of phase transitions with quenched disorder. We also compare our findings with previous work on this and related problems; and we consider experiments.

The two-dimensional site-diluted  $O(3)$  rotor model has two quantum phase transitions, (i) a generic transition for dilutions  $p$  below the percolation threshold  $p_c$  of the lattice and (ii) a quantum percolation transition at  $p_c$ . These transitions are separated by a multicritical point. Our calculations have shown that the critical behavior of all these transitions is of conventional power-law type. In

| Exponent     | Generic  | Multicritical | Percolation | Perc. (theory) |
|--------------|----------|---------------|-------------|----------------|
| $z$          | 1.310(6) | 1.54(2)       | 1.83(3)     | 91/48          |
| $\beta/\nu$  | 0.53(3)  | 0.40(3)       | 0.15(3)     | 5/48           |
| $\gamma/\nu$ | 2.26(6)  | 2.71(3)       | 3.51(5)     | 59/16          |
| $\nu$        | 1.16(3)  |               |             |                |

TABLE I: Numerical results for the critical exponents. For the generic transition, the values are from the combined fit of all four datasets for dilutions 1/8, 1/5, 2/7, and 1/3. For the multicritical point and the percolation transition the values are from straight power-law fits. The numbers in brackets give the *statistical* error of the last given digits. For the percolation transition we also give the theoretical results from Ref. 55. The numerical data are compatible with these values if one allows for corrections to scaling.

contrast, the Ising version of our model, the diluted 2d random transverse-field Ising model, shows an infinite-randomness critical point.<sup>15,25,56</sup> To study the generic transition, we have considered four different dilutions. Combined fits of all data sets have allowed us to systematically include corrections to scaling. In this way, we have provided strong evidence that the critical behavior of the generic transition is universal, i.e., independent of the dilution. Because of the high numerical effort, we have considered only one data set for the percolation transition. This one data set does not allow us to extract the leading exponents *and* the corrections to scaling from a free fit of the numerical data. However, including corrections to scaling when fitting the data to the theory of Ref. 55 leads to a very good agreement. For the multicritical point, there is only one data set, and no quantitative theoretical results exist. Therefore, our results for the multicritical behavior are on somewhat less firm ground because they do not contain corrections to scaling. Our exponent values are summarized in table I.

Recently, a general classification has been suggested for phase transitions with weak (random- $T_c$  type) quenched disorder and short-range interactions.<sup>35,45</sup> According to this classification, the type of critical behavior depends on the effective dimensionality  $d_{RR}$  of the defects or, equivalently, the rare regions. Three cases can be distinguished. (A) If  $d_{RR}$  is below the lower critical dimension  $d_c^-$  of the problem, rare region effects are exponentially small. As a result, the transition is sharp, and the critical point is of conventional power-law type. (B) In the second class, with  $d_{RR} = d_c^-$ , rare regions are much more important. A sharp transition still exists, but the critical point is controlled by an infinite-randomness fixed point with activated scaling. In addition, there are strong power-law Griffiths effects. (C) Finally, for  $d_{RR} > d_c^-$ , the rare regions can order independently leading to a destruction of the sharp phase transition by smearing.

In the problem considered here,  $d_{RR} = 1$  because the defects are linear. The lower critical dimension of the Heisenberg universality class is  $d_c^- = 2$ . Therefore,  $d_{RR} < d_c^-$ , and our model should be in class A with conventional power-law critical behavior. Our numerical

results are thus in complete agreement with the above general rare-region based classification scheme.

Let us compare our results to previous work. The qualitative structure of the phase diagram, viz., the fact that long-range order survives for all dilutions up to and including the percolation threshold agrees with earlier quantum Monte-Carlo simulations for the bilayer quantum Heisenberg antiferromagnet<sup>41,42</sup> and with analytical results for diluted magnets<sup>57</sup> as well as  $O(2)$  rotors.<sup>58</sup> Sandvik<sup>41</sup> and Vajk and Greven<sup>42</sup> studied the multicritical point at  $p = p_c$ . They found a dynamical exponent of  $z \approx 1.3$  significantly lower than our result of 1.54. More recently, Sandvik<sup>59</sup> reported a somewhat larger value of  $z = 1.36$ , but it is still well below our result. The reasons for this discrepancy are presently not fully understood. Possible explanations include a failure of the quantum to classical mapping (which we consider unlikely) and corrections to scaling of the lattice percolation problem. In this context it is worth noting that the scaling properties of the lattice enter our calculations in a different way than that of Ref. 59. Our analysis of the Binder ratio works with linear extensions in space and time directions, directly giving  $z$ . In contrast, Ref. 59 analyzes the temperature dependence of the susceptibility and effectively measures  $D_f/z$  with  $D_f$  being the fractal dimension of the percolation cluster. It is clear that corrections to scaling, if any, will enter the two calculations very differently. Vajk and Greven<sup>42</sup> also quoted exponents for  $p < p_c$ . At dilution  $p = 0.25$  they find  $z = 1.07$  and  $\nu = 0.89$ , different from our results. However, as the authors of Ref. 42 pointed out, a value of  $\nu < 1$  violates the Harris criterion, indicating that it represents an effective rather than an asymptotic exponent. It would also be useful to compare our exponents with analytical results. To the best of our knowledge, the only quantitative result for the generic transition is a resummation of the 2-loop  $\epsilon$ -expansion.<sup>60</sup> The predicted exponents significantly differ from ours; but they also violate the Harris criterion, casting doubt on their validity. While no quantitative analytical results exist for the multicritical point, there is a complete scaling theory for the percolation transition,<sup>55</sup> and the exponents in two dimensions are known exactly. Our numerical data are in excellent agreement with the

exact values if one allows for corrections to scaling. (Even if corrections to scaling are not included, the differences between the theoretical and numerical exponent values are only a few percent.)

Finally, we discuss experiments. Chemical doping, i.e., random replacement of magnetic by non-magnetic ions, e.g., Cu by Zn in  $\text{YBa}_2\text{Cu}_3\text{O}_6$ , in both single-layer and bilayer antiferromagnets realizes site rather than dimer dilution. As discussed at the end of section II A, this leads to random Berry phases and a completely different physical picture. The most promising way to achieve dimer dilution is the introduction of strong antiferromagnetic intra-dimer bonds at random locations. Thus we propose to study magnetic transitions in bond-disordered systems; those transitions can be expected to be in the same universality class as the one studied here. One candidate material – albeit 3d – is  $(\text{Tl,K})\text{CuCl}_3$ <sup>61</sup> under pressure; interesting quasi-2d compounds are  $\text{SrCu}_2(\text{BO}_3)_2$  or  $\text{BaCuSi}_2\text{O}_6$ , where suitable dopants remain to be found. Our results may also be interesting for some single-layer Zn doped cuprate antiferromagnets that have been speculated to be parametrically close to the multicritical point of the rotor model.<sup>41,42</sup> Moreover, the qualitative properties of the phase diagram and the critical behavior are also important for disordered Josephson junction arrays or diluted bosons in optical lattices.

### Acknowledgements

We thank Matthias Vojta for a collaboration in the early stages of this work. We have also benefitted from discussions with Stephan Haas, Martin Greven, Anders Sandvik, and Joerg Schmalian. This work has been supported in part by the NSF under grant nos. DMR-0339147 and PHY99-07949, by Research Corporation, by NSERC of Canada, and by the University of Missouri Research Board. We are also grateful for the hospitality of the Aspen Center for Physics and the Kavli Institute for Theoretical Physics, Santa Barbara where parts of this work have been performed.

<sup>1</sup> W. Wu, B. Ellman, T. F. Rosenbaum, G. Aeppli, and D. H. Reich, *Phys. Rev. Lett.* **67**, 2076 (1991).

<sup>2</sup> W. Wu, D. Bitko, T. F. Rosenbaum, and G. Aeppli, *Phys. Rev. Lett.* **71**, 1919 (1993).

<sup>3</sup> C. L. Seaman, M. B. Maple, B. W. Lee, S. Ghamaty, M. S. Torikachvili, J. S. Kang, L. Z. Liu, J. W. Allen, and D. L. Cox, *Phys. Rev. Lett.* **67**, 2882 (1991).

<sup>4</sup> B. Andraka and A. M. Tsvetlik, *Phys. Rev. Lett.* **67**, 2886 (1991).

<sup>5</sup> M. C. de Andrade, R. Chau, R. P. Dickey, N. R. Dille, E. J. Freeman, D. A. Gajewski, M. B. Maple, R. Movshovich, A. H. Castro Neto, G. Castilla, et al., *Phys.*

*Rev. Lett.* **81**, 5620 (1998).

<sup>6</sup> G. Stewart, *Rev. Mod. Phys.* **73**, 797 (2001).

<sup>7</sup> J. F. DiTusa, S. Guo, D. P. Young, R. T. Macaluso, N. L. Henderson, and J. Y. Chan (2003), cond-mat/0306541.

<sup>8</sup> J. P. Attfield, A. L. Kharlanov, and J. A. McAllister, *Nature* **394**, 157 (1998).

<sup>9</sup> C. Panagopoulos, J. L. Tallon, B. D. Rainford, T. Xiang, J. R. Cooper, and C. A. Scott, *Phys. Rev. B* **66**, 064501 (2002).

<sup>10</sup> E. Abrahams, S. Kravchenko, and M. Sarachik, *Rev. Mod. Phys.* **73**, 251 (2001).

<sup>11</sup> S. V. Kravchenko, W. E. Mason, G. E. Bowker, J. E.

- Furieux, V. M. Pudalov, and M. Dlorio, Phys. Rev. B **51**, 7038 (1995).
- <sup>12</sup> A. F. Hebard and A. A. Paalanen, Phys. Rev. Lett. **65**, 927 (1990).
- <sup>13</sup> G. Grinstein, in *Fundamental Problems in Statistical Mechanics VI*, edited by E. G. D. Cohen (Elsevier, New York, 1985), p. 147.
- <sup>14</sup> A. B. Harris, J. Phys. C **7**, 1671 (1974).
- <sup>15</sup> O. Motrunich, S. C. Mau, D. A. Huse, and D. S. Fisher, Phys. Rev. B **61**, 1160 (2000).
- <sup>16</sup> A. Aharony and A. B. Harris, Phys. Rev. Lett. **77**, 3700 (1996).
- <sup>17</sup> S. Wiseman and E. Domany, Phys. Rev. Lett. **81**, 22 (1998).
- <sup>18</sup> D. S. Fisher, Phys. Rev. Lett. **69**, 534 (1992).
- <sup>19</sup> D. S. Fisher, Phys. Rev. B **51**, 6411 (1995).
- <sup>20</sup> J. Hertz, Phys. Rev. B **14**, 1165 (1976).
- <sup>21</sup> S. Sachdev, *Quantum phase transitions* (Cambridge University Press, Cambridge, 1999).
- <sup>22</sup> A. P. Young and H. Rieger, Phys. Rev. B **53**, 8486 (1996).
- <sup>23</sup> B. M. McCoy and T. T. Wu, Phys. Rev. Lett. **21**, 549 (1968).
- <sup>24</sup> B. M. McCoy, Phys. Rev. Lett. **23**, 383 (1969).
- <sup>25</sup> C. Pich, A. P. Young, H. Rieger, and N. Kawashima, Phys. Rev. Lett. **81**, 5916 (1998).
- <sup>26</sup> M. Thill and D. Huse, Physica A **214**, 321 (1995).
- <sup>27</sup> H. Rieger and A. P. Young, Phys. Rev. B **54**, 3328 (1996).
- <sup>28</sup> R. B. Griffiths, Phys. Rev. Lett. **23**, 17 (1969).
- <sup>29</sup> M. Randeria, J. Sethna, and R. G. Palmer, Phys. Rev. Lett. **54**, 1321 (1985).
- <sup>30</sup> T. Vojta, Phys. Rev. Lett. **90**, 107202 (2003).
- <sup>31</sup> T. Vojta, J. Phys. A **36**, 10921 (2003).
- <sup>32</sup> R. Sknepnek and T. Vojta, Phys. Rev. B **69**, 174410 (2004).
- <sup>33</sup> T. Vojta, Phys. Rev. E **70**, 026108 (2004).
- <sup>34</sup> M. Dickison and T. Vojta, J. Phys. A **38**, 1199 (2005).
- <sup>35</sup> T. Vojta, J. Phys. A **39**, R143 (2006).
- <sup>36</sup> D. S. Fisher, Phys. Rev. B **50**, 3799 (1994).
- <sup>37</sup> Y. C. Lin, R. Melin, H. Rieger, and F. Igloi, Phys. Rev. B **68**, 024424 (2003).
- <sup>38</sup> N. Laflorencie, S. Wessel, A. Läuchli, and H. Rieger, Phys. Rev. B **73**, 060403 (2006).
- <sup>39</sup> A. Sandvik, Phys. Rev. Lett. **86**, 3209 (2001).
- <sup>40</sup> A. Sandvik, Phys. Rev. B **66**, 024418 (2002).
- <sup>41</sup> A. Sandvik, Phys. Rev. Lett. **89**, 177201 (2002).
- <sup>42</sup> O. P. Vajk and M. Greven, Phys. Rev. Lett. **89**, 177202 (2002).
- <sup>43</sup> R. Yu, T. Roscilde, and S. Haas, Phys. Rev. B **73**, 064406 (2006).
- <sup>44</sup> R. Sknepnek, T. Vojta, and M. Vojta, Phys. Rev. Lett. **93**, 097201 (2004).
- <sup>45</sup> T. Vojta and J. Schmalian, Phys. Rev. B **72**, 045438 (2005).
- <sup>46</sup> S. Sachdev and M. Vojta, in *Proceedings of the XIII International Congress on Mathematical Physics*, edited by A. Fokas (International Press, Boston, 2001).
- <sup>47</sup> M. Guo, R. Bhatt, and D. Huse, Phys. Rev. Lett. **72**, 4137 (1994).
- <sup>48</sup> H. Rieger and A. P. Young, Phys. Rev. Lett. **72**, 4141 (1994).
- <sup>49</sup> U. Wolff, Phys. Rev. Lett. **62**, 361 (1989).
- <sup>50</sup> W. Selke, L. N. Shchur, and A. L. Tapalov, in *Annual Reviews of Computational Physics*, edited by D. Stauffer (World Scientific, Singapore, 1994), vol. 1.
- <sup>51</sup> H. G. Ballesteros, L. A. Fernandez, V. Martin-Mayor, A. M. Sudupe, G. Parisi, and J. J. Ruiz-Lorenzo, Phys. Rev. B **58**, 2740 (1998).
- <sup>52</sup> H. G. Ballesteros, L. A. Fernandez, V. Martin-Mayor, A. M. Sudupe, G. Parisi, and J. J. Ruiz-Lorenzo, Nucl. Phys. B **512**, 681 (1998).
- <sup>53</sup> F. Cooper, B. Freedman, and D. Preston, Nucl. Phys. B **210**, 210 (1982).
- <sup>54</sup> J. K. Kim, Phys. Rev. Lett. **70**, 1735 (1993).
- <sup>55</sup> T. Vojta and J. Schmalian, Phys. Rev. Lett. **95**, 237206 (2005).
- <sup>56</sup> T. Senthil and S. Sachdev, Phys. Rev. Lett. **77**, 5292 (1996).
- <sup>57</sup> E. R. Mucciolo, A. H. Castro Neto, and C. Chamon, Phys. Rev. B **69**, 214424 (2004).
- <sup>58</sup> N. Bray-Ali, J. E. Moore, T. Senthil, and A. Vishwanath, Phys. Rev. B **73**, 064417 (2006).
- <sup>59</sup> A. Sandvik, Phys. Rev. Lett. **96**, 207201 (2006).
- <sup>60</sup> V. Blavatska, C. von Ferber, and Y. Holovatch, Phys. Rev. B **67**, 094404 (2003).
- <sup>61</sup> A. Oosawa and H. Tanaka, Phys. Rev. B **65**, 184437 (2002).
- <sup>62</sup> Because the  $m(L)$  curves do not deviate strongly from power-law behavior, letting  $\omega$  vary does not lead to a stable fit.